Visualizing strongly-correlated electrons with a novel scanning tunneling microscope

Battisti, I.

6

Quasiparticle interference in the correlated metal Sr_2RhO_4

6.1 Introduction

SI-STM directly probes real space, but in metals or superconductors with sharp quasiparticles, it can also provide information about momentum space. This is possible by imaging the interference of standing waves that are caused by the scattering of quasiparticles. A general introduction to this technique, called *quasiparticle interference imaging*, is given in chapter 2, Sec. 2.3.

The most popular probe to access momentum space information is angle-resolved photoemission spectroscopy (ARPES), also a surface-sensitive technique. ARPES directly measures photon-induced quasiparticle excitations, resolving both energy and momentum. It can therefore measure the band structure of materials.

Because both STM and ARPES have advantages and disadvantages related to their experimental realizations, it is recommendable to combine their results in order to obtain a better understanding of the underlying physics. ARPES has the clear advantage of probing momentum space directly, while STM measures the scattering vectors of quasiparticles. However, ARPES probes only states below the Fermi level, and its best energy resolution is a few meV, limited by temperature. STM, on the other hand, can probe states both above and below the Fermi level, and because it can be performed at much lower temperatures, the energy resolution can be lower. For example, at 250 mK, the energy resolution is $\Delta E_{\mathrm{STM}} \sim 75\,\mu\mathrm{eV}$ (see Sec. 2.5 for details). Thanks to its superior energy resolution, STM has been able, for instance, to detect k-space anisotropy in iron-based superconductors previously invisible to ARPES [138, 139], and to image the band structure of heavy fermions materials where ARPES cannot access the energy scales [37, 38]. Quasiparticle interference imaging also brought enormous insights in the superconducting phase of cuprate high-T_c superconductors [18, 34]. However, in general QPI imaging is a difficult experimental technique, and its theoretical understanding is still in progress [140, 141].

Both STM and ARPES measure quantities proportional to the quasiparticle spectral function, as explained in section 2.3.1. Because the two techniques in principle have access to the same physical information, it is natural to try to compare their results. However, the comparison between the two is not always simple. While they generally agree on the main observed features, they very often differ in the details, as it was shown for example for cuprates [45–47], and for the normal state of Sr_2RuO_4 [43]. In both these systems, the two techniques obtain very similar Fermi surfaces, but different slopes in the energy-momentum dispersions. Discrepancies could be caused by measurements effects in both techniques, i.e., the tunneling/photoemission matrix elements, tip-induced effects, and photon energy and polarization, however they could also be related to more intrinsic factors.

Here, we use quasiparticle interference to study the electronic structure of the correlated metal Sr_2RhO_4, which is an example of an almost perfect Fermi liquid [68]. This material has very sharp quasiparticles and a simple band structure, and it is therefore relatively easy to study with quasiparticle interference. This makes it a good candidate to better understand how STM QPI can be related to ARPES results. Additionally, we study samples belonging to the same batch used in published ARPES and quantum oscillation studies [68, 69], which makes the comparison more sound.

We start with an introduction to the material and to the relevant literature, and then proceed with the presentation of our experimental results. Finally, we compare our data to ARPES results. The data that we show here is the first data that we acquire with our home-built microscope, described in chapter 3. While the data quality is good enough to have some preliminary conclusions, further measurements are needed and planned in order to confirm our findings. We will come back to this while discussing the results and in the conclusions.

6.2 The correlated metal Sr_2RhO_4

The rhodate Sr_2RhO_4 has a tetragonal crystal structure isostructural to the cuprate La_2CuO_4. The RhO_6 octahedra are additionally rotated of 11° around the c-axis, as shown in Fig. 6.1a. Sr_2RhO_4 has therefore an identical structure to the iridate Sr_2IrO_4 that has been discussed in chapter 4.

The octahedra rotation causes the formation of a new orthorhombic unit cell and, consequently, a reduction of the first Brillouin zone, as illustrated in Fig. 6.1b-c. The lattice parameters of the new orthorhombic cell are $a^* = \sqrt{2}a = 5.45\,\text{Å}$ and $c^* = 2c = 25.7\,\text{Å}$, where a and c are the lattice parameters of the undistorted structure [142].

In the periodic table, Rh belongs to $4d$ transition metals. With its odd number of electrons per unit cell (electronic configuration $4d^5$), Sr_2RhO_4 is a metal, as it is expected from simple band structure considerations. Nevertheless, Coulomb correlations U and spin-orbit coupling λ are present in this material as well, and only by taking them into account can the experimentally observed Fermi surface be reproduced by LDA calculations [69, 143, 144].

The most studied $4d$ transition metal oxides are probably the ruthenates Sr_2RuO_4 and $Sr_3Ru_2O_7$. In particular, Sr_2RuO_4 is famous for showing spin-triplet superconductivity below 1.5 K [145]. In the normal state, Sr_2RuO_4 is also a strongly two-dimensional Fermi liquid, with a Fermi surface characterized by three cylindrical sheets, called α (which is hole like), β and γ (which are electron like), as shown in Fig 6.2a. Calculations show that α and β are strongly one-dimensional and are derived from the Ru

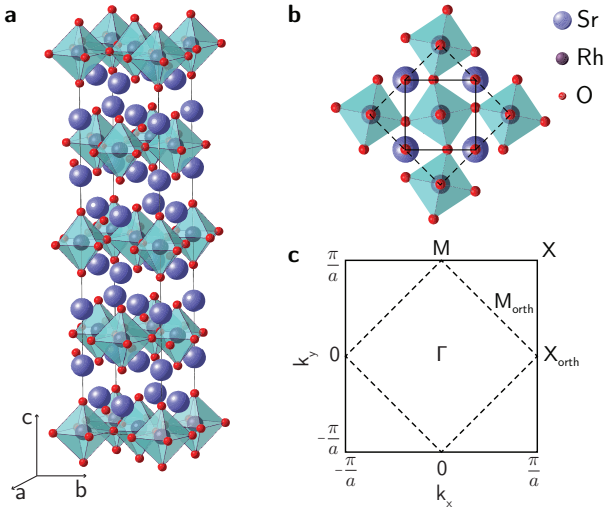

Figure 6.1: **a**, Crystal structure. **b**, Top view of the crystal structure showing the orthorhombic distortion. **c**, First Brillouin zone and reduced BZ due to orthorhombicity. The high symmetry directions Γ, X and M are indicated for both undistorted and distorted structure.

$4d_{xz,yz}$ orbitals, while γ is dominantly two-dimensional, derived from the $4d_{xy}$ orbital [145].

Rhodium has just one atom more than ruthenium, but its electronic structure is quite different. In a naïve picture, one could think to obtain the Fermi surface of Sr_2RhO_4 simply by shifting the Sr_2RuO_4 band structure to accommodate the extra electron of Rh. However, spectroscopic studies, later confirmed by theory, show that Sr_2RhO_4 has only two bands at the Fermi level [69, 143], respectively the α and β bands. In addition, they are back-folded due to the first Brillouin zone reduction caused by the octahedra rotation[1], as shown in Fig. 6.2b. It has been shown that the octahedra rotation is also responsible for the absence of the γ band from the Fermi surface: the structural distortion combined with the folding of the bands causes an additional hybridization of the occupied d_{xy} orbital with the unoccupied $d_{x^2-y^2}$ orbital, which mixes the bands and opens a gap between the two, pushing the d_{xy} band below the Fermi level [143]. The physics of the material is therefore governed by the three electrons per Rh atom that are left at the Fermi level, distributed between the α and β bands.

We will now introduce a brief summary of the most prominent experimental studies that have been performed on the rhodate Sr_2RhO_4, with a focus on photoemission

[1] Sr_2RuO_4 has an undistorted crystal structure, with a normal tetragonal unit cell. Upon cleaving it shows a surface reconstruction with the octahedra rotating by 11° in the top layer only, as for example shown by Ref. [43].

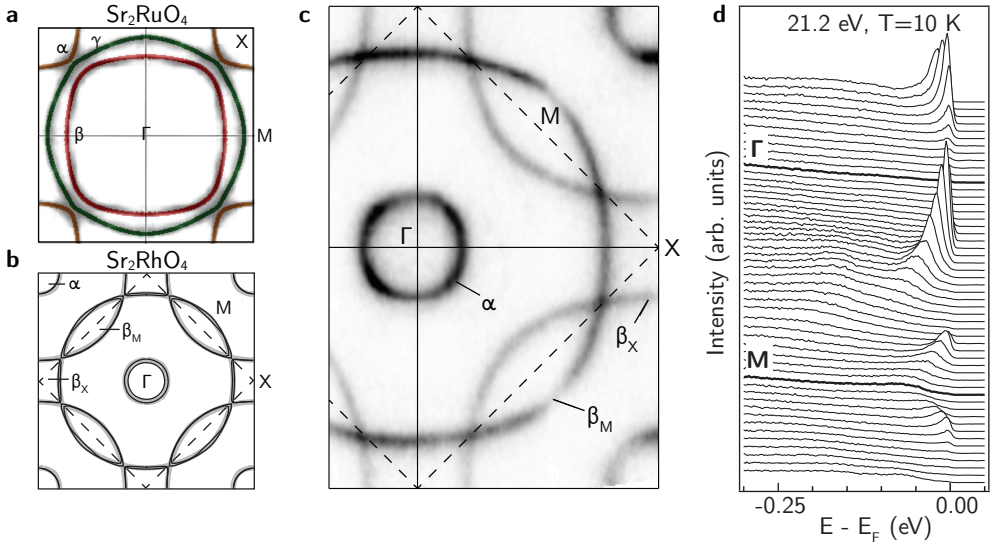

Figure 6.2: **a**, Fermi surface of Sr_2RuO_4, reproduced from Ref. [146]. **b**, Fermi surface of Sr_2RhO_4 as obtained by LDA+SOC+U calculations, reproduced from Ref. [144]. **c**, Fermi surface of Sr_2RhO_4 measured with ARPES at 10 K, reproduced from Ref. [69]. **d**, ARPES spectra along the ΓM direction of the orthorhombic Brillouin zone, reproduced from Ref. [69].

spectroscopy. Later in the chapter, we will compare our STM experimental results to these studies.

We start with crystal growth and transport properties, which have mainly been reported in Ref. [68]. Sr_2RhO_4 single crystals can be grown by the floating zone technique, with the formation of big crystals up to 1.5 cm long. Subsequent annealing in O_2 atmosphere is necessary to improve the quality of the crystals, leading to low-temperature in-plane resistivities $\rho_{ab} < 7\,\mu\Omega\,\mathrm{cm}$. The out of plane resistivity ρ_c is about three orders of magnitude higher, confirming the strongly two-dimensional nature of the electronic structure. The low in-plane residual resistivity is a hallmark of extremely high purity crystals, similar to what is achieved in Sr_2RuO_4. This allows the measurement of quantum oscillations, that are unobservable in most oxide metals due to signal suppression from impurity scattering [68].

Angle-resolved photemission spectroscopy (ARPES) provides an essential contribution to the understanding of the electronic structure of Sr_2RhO_4 [68, 69, 143]. In Fig. 6.2c-d, we reproduce ARPES data from Ref. [69]. The Fermi surface clearly shows the slightly asymmetric hole-like α band and electron-like β band, as well as their copies that are back folded along the orthorhombic zone boundary (dashed line in Fig. 6.2c). A closer investigation of the data reveals that a small gap opens at the crossing of the β band with its back folded copy at the orthorhombic zone bound-

ary, causing the formation of three different pockets at the Fermi surface: the central hole pocket (α), the lens-shaped electron pockets around the M point (β_M) and the square-shaped hole pockets around the X point (β_X). The volume of the pockets as extracted from the ARPES data leads to a total Luttinger volume[2] of three electrons per Rh atom, confirming the picture of a fully occupied γ band.

6.3 SI-STM quasiparticle interference measurements

The sharpness of the quasiparticles that are measured on Sr_2RhO_4 by ARPES and quantum oscillations makes the material a very good candidate for the imaging of quasiparticle interference with STM [70]. In the following, we report our SI-STM measurements on the same Sr_2RhO_4 samples of which growth and measurements are reported in Ref. [68, 69] and summarized in section 6.2. This allows for a direct comparison with ARPES results.

A general explanation of the techniques of quasiparticle interference imaging and Fourier transform STM is given in section 2.3, where we introduce many concepts that are used in the present chapter.

The measurements shown here have been performed with our home-built STM described in chapter 3. The samples are about 2−3 mm in lateral size, and cleave very easily. They are cleaved in situ at ≈20 K, and immediately transferred to the STM head. STM measurements are performed at the base temperature of 4.3 K with a chemically etched tungsten tip that has been previously prepared by field emission on a gold surface. STM topographs are taken in the constant current mode, and the $\mathrm{d}I/\mathrm{d}V$ spectra are collected using a standard lock-in technique with modulation frequency $f = 863$ Hz.

While the data quality we achieve from the very first measurement is confirming the exceptional performance of the microscope in terms of signal-to-noise ratio, it is not yet ideal. In particular, the tip apex shape is not perfect, and we encountered an asymmetry of the piezotube polarization. We can partially remove these effects by post-processing the data, as we explain throughout the chapter. However, to confirm our findings and accumulate more statistics, additional measurements are planned.

In Fig. 6.3a, we show a STM topograph acquired on Sr_2RhO_4. The material, similarly to Sr_2IrO_4, cleaves between SrO layers, and the Sr atoms are visible on the surface with spacing $a = 3.85$ Å. Two different types of defects are visible, and are identified based on Ref. [147]: (i) square-shaped defects, corresponding to a missing Sr atom; (ii) cross-shaped defects, centered at the position of an O atom and corresponding to

[2]Luttinger's theorem states that the volume enclosed by a material's Fermi surface is directly proportional to the particle density. Importantly, this is not changed by the presence of electron-electron interactions.

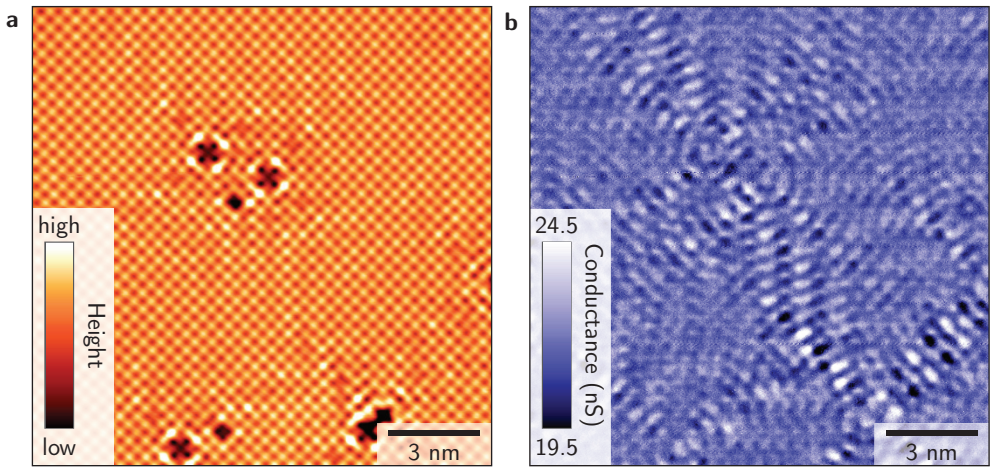

Figure 6.3: Quasiparticle interference in real space. **a**, Topograph on Sr_2RhO_4 on a field of view of $15\times15\,nm^2$. The setup conditions are ($V_b = -20\,meV$, $I_t = 600\,pA$). **b**, Conductance layer at $E = -20\,meV$ acquired simultaneously to the topograph in panel **a** with bias modulation amplitude $dV = 2\,meV$.

a chemisorbed CO molecule, where the carbon atom gets incorporated in the surface by replacing the apical oxygen atom. The cross-shaped defects show two possible orientations, depending on the rotation of the octahedra to which they are bound. In Fig. 6.3b, we show the conductance layer at $-20\,meV$ acquired simultaneously to the topograph in Fig. 6.3a, where quasiparticle interference is imaged in real space. The lattice defects obviously act as scattering centers, creating an interference pattern between the quasiparticles standing waves. Such an image contains quantitative information about the quasiparticles momenta and, therefore, the band structure, as already introduced in chapter 2.3. The easiest way to access this information is by taking two-dimensional Fourier transforms of the conductance layers, to create momentum space images of the quasiparticle scattering vectors $\mathbf{q}$.

In order to obtain high quality q-space images (i.e. high signal-to-noise ratio and resolution), one needs to scan over a bigger field of view than the one showed in Fig. 6.3, eventually reducing the real space resolution. We show an example of a spectroscopic map that is optimized for Fourier space analysis in Fig. 6.4. The field of view is $55\times55\,nm^2$ and it is measured with 288×288 pixels. Several lattice defects are visible on the topograph. They create a very rich QPI pattern in the conductance layers, as shown for the energy layer corresponding to the Fermi level in Fig. 6.4b.

In Fig. 6.4c, we plot the two-dimensional Fourier transform of Fig. 6.4b. The field of view is rotated by 45° in order to have the same orientation of ARPES data and theoretical calculations. Several features can be observed. The Bragg peaks corre-

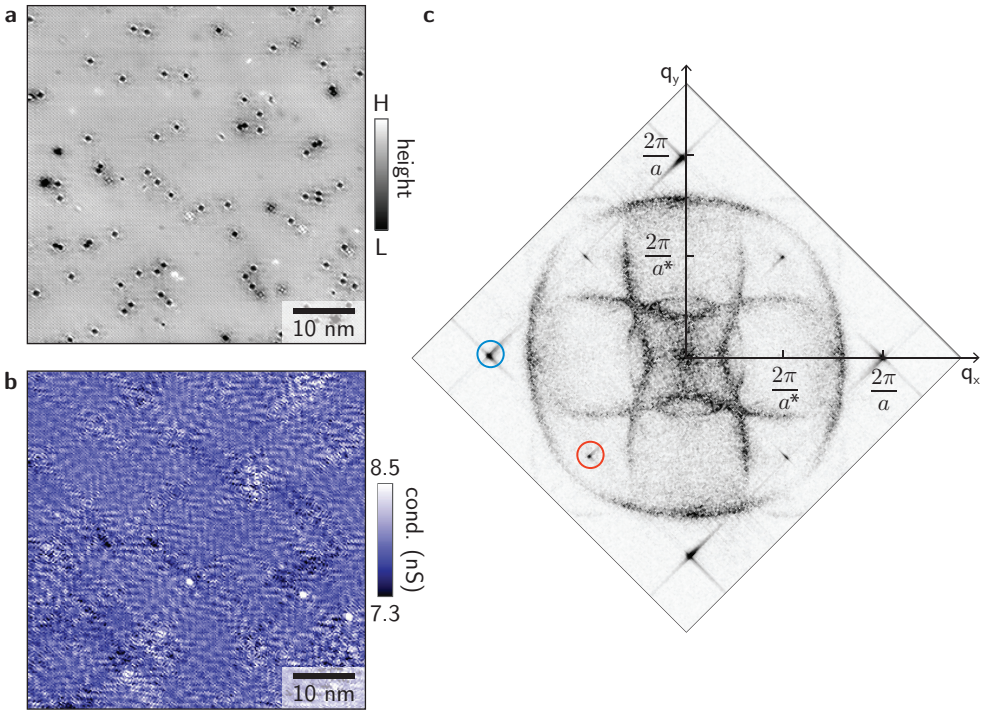

Figure 6.4: Spectroscopic map on Sr_2RhO_4. Field of view $55\times55\,nm^2$, 288×288 pixels. Setup conditions ($V_b = -50$ meV, $I_t = 500$ pA). **a**, Topograph. **b**, Conductance layer at E=0 meV, showing QPI in real space (raw data). **c**, Fourier transform of panel **b**, rotated by 45° (raw data). The Bragg peaks corresponding to the orthorhombic unit cell and to the Sr lattice periodicity are indicated with red and blue circles, respectively.

sponding to both the orthorhombic unit cell and the surface Sr lattice are indicated by the red and the blue circles, respectively. All the other features stem from quasiparticles scattering between high density of states areas of the Fermi surface, and their origin will be discussed in the rest of the chapter.

The image shown in Fig. 6.4c shows the raw Fourier transform. It is slightly distorted due to an asymmetry in the piezotube polarization and a slightly double tip, combined with a minimal thermal drift. Before extracting quantitative information from the data, we correct the images for the distortions. Additionally, we four-fold symmetrize the Fourier-transformed images, to remove residual asymmetries and improve the signal-to-noise ratio[3].

[3]To get an idea of how much distortion corrections and symmetrization change the Fourier transformed images, Fig. 6.4c (raw) should be compared with Fig. 6.6e (corrected).

6.4 Identification of scattering vectors: comparison with simulations

In order to analyze the origin of the features seen in the QPI measurements, we compute the autocorrelation of the Fermi surface, following the joint density of states (JDOS) approach introduced in section 2.3. In autocorrelation images, high intensity corresponds to scattering vectors that connect parallel regions of the Fermi surface, allowing a direct comparison with the STM q-space images.

To reproduce the Fermi surface measured with ARPES in Ref. [69], we compute the band structure from a minimal 2D tight-binding model adapted from Ref. [148]. It includes only the bands derived from the d_{xz} and d_{yz} orbitals, neglecting the γ band deriving from the d_{xy} orbital. The model uses two sublattices A, B to reproduce the band folding due to the octahedra rotation, and ignores next-nearest-neighbors hopping processes. The resulting 4×4 tight-binding hamiltonian is:

$$H = \begin{bmatrix} H_{SO} & H_{AB} \\ H_{AB}^{\dagger} & H_{SO} \end{bmatrix}, \tag{6.1}$$

where the on-site spin-orbit interaction H_{SO} and the nearest-neighbor hopping H_{AB} are given by

$$H_{SO} = \begin{bmatrix} 0 & i\lambda/2 \\ -i\lambda/2 & 0 \end{bmatrix}, \qquad H_{AB} = \begin{bmatrix} \epsilon_{yz} & \epsilon_{rot} \\ -\epsilon_{rot} & \epsilon_{xz} \end{bmatrix}. \tag{6.2}$$

Here, λ is the spin-orbit coupling constant, and it plays the role of mixing the d_{xz} and d_{yz} orbitals. The hopping is governed by the dispersions ϵ_{yz}, ϵ_{xz}, ϵ_{rot}, that are given by:

$$\epsilon_{yz} = -2t_{\pi}\cos(k_y) - 2t_{\delta}\cos(k_x), \tag{6.3}$$

$$\epsilon_{xz} = -2t_{\pi}\cos(k_x) - 2t_{\delta}\cos(k_y), \tag{6.4}$$

$$\epsilon_{rot} = -2t_{p}\cos(k_y) - 2t_{p}\cos(k_x). \tag{6.5}$$

Here, the terms t_{π} and t_{δ} represent hopping between identical orbitals on neighboring Rh sites (respectively, $yz \rightarrow yz$ and $xz \rightarrow xz$), while t_p allows hopping between different orbitals (e.g. $yz \rightarrow xz$) due to the octahedra rotation. The model has five parameters: the three hopping terms, the spin-orbit coupling and the Fermi energy: $(t_{\pi}, t_{\delta}, t_p, \lambda, E_F)$. We optimize the parameters in order to reproduce the ARPES band structure from Ref. [69], to obtain $(t_{\pi}, t_{\delta}, t_p, \lambda, E_F) = (0.104, 0.012, 0.0314, 0.14, 0.155)$.

By diagonalizing the hamiltonian in Eq. (6.1) with the given parameters, we obtain the tight-binding band structure. From the tight-binding constant energy contours,

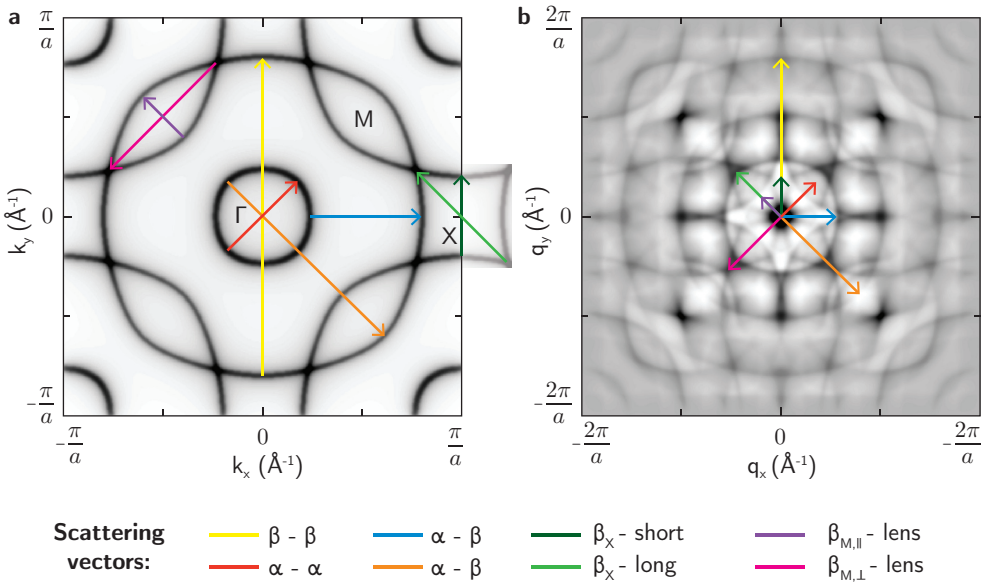

Figure 6.5: **a**, Simulated Fermi surface computed using the tight-binding model discussed in the main text. **b**, Autocorrelation of the Fermi surface in panel **a**. The main scattering vectors are indicated with the same color coding in both panels. Note the different axes.

we generate a rough simulated $A(\mathbf{k}, \omega)$. To reproduce ARPES experimental energy and momentum resolution, we add energy layers in an energy window corresponding to the ARPES energy resolution and we apply a Lorentzian smoothing in k-space.

The resulting simulated Fermi surface is shown in Fig. 6.5a. The most prominent scattering vectors are indicated by arrows. The main scattering vectors correspond to the $\alpha - \alpha$ (red) and $\beta - \beta$ (yellow) intraband scatterings and to two possibilities for the $\alpha - \beta$ interband scattering (orange and blue). In addition, we indicate vectors connecting the backfolded copies of the bands, within the lens-shaped β_M pocket (purple) and within the square-shaped β_X pocket (green).

In Fig. 6.5b, we show the computed autocorrelation from Fig. 6.5a, where the scattering vectors from the Fermi surface are identified by the same color coding. The autocorrelation shows much more details than the STM QPI data in Fig. 6.4c. This is probably because the simplistic autocorrelation approach neglects scattering probabilities due to matrix elements. It is, nevertheless, useful for the identification of the features seen in QPI data.

In order to have a more complete overview of the energy evolution, we show in Fig. 6.6 a selection of layers from the same spectroscopic map shown in Fig. 6.4. The data,

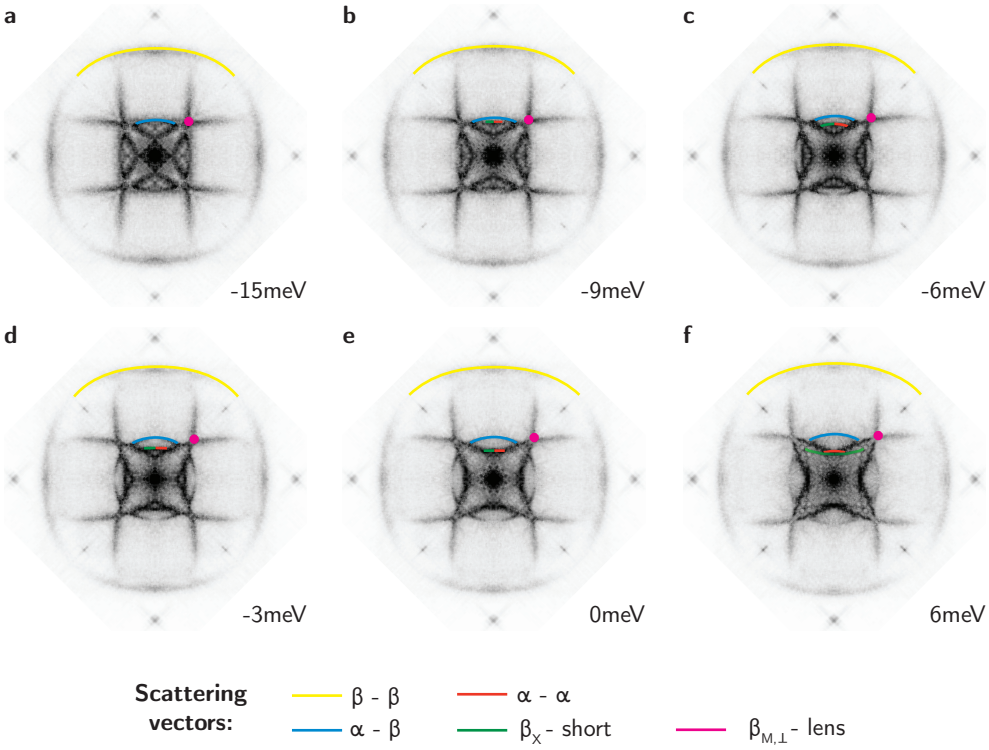

Figure 6.6: a-f Fourier transform of selected conductance layers of the same spectroscopic map shown in Fig. 6.4. The field of view is $55\times55\,\mathrm{nm}^2$, with 288×288 pixels. The setup conditions are ($V_b = -50$ meV, $I_t = 500$ pA), and the map has 11 energy layers between -15 meV and 15 meV spaced by 3 meV intervals. The real space data is corrected for drift and other distortions and the Fourier transform is 4-fold symmetrized to ease the visualization of the features.

here, is corrected for drift and piezotube miscalibration and additionally four-fold symmetrized to ease the identification.

From a careful comparison of the scattering vectors, we can identify several features in the QPI data in Fig. 6.6. The biggest circular feature corresponds to the $\beta - \beta$ intraband scattering. It grows in diameter with increasing energy, indicating its electron-like character. We can also identify the smaller $\alpha - \beta$ interband scattering (blue), while the bigger $\alpha - \beta$ interband scattering (orange arrow in Fig. 6.5) is completely absent from the QPI data. At small $\mathbf{q}$, we find the scattering vectors corresponding to the lens-shaped β_M electron pockets (magenta dot), also growing with increasing energy. The scattering vectors within the hole-like features (α and β_X pockets) are instead more difficult to identify. There is a clear signal of a hole-like feature along the ΓX direction that shrinks with energy. However it is not possible to discern whether it belongs to the α (red) or to the β_X (green) hole pocket, since along this direction

both pockets have very similar sizes, and where their shapes start to differ, the signal is partially hidden from the lens-shaped β_M pockets. We show in Sec. 6.5 that the two hole pockets can be distinguished along the ΓM direction.

6.5 Extraction of dispersions and Fermi vectors

To better characterize the dispersion of the scattering vectors, we take (E, **q**) cuts along the high symmetry directions ΓX and ΓM, as shown in Fig. 6.7 for two different measurements. Before taking the cuts, the Fourier transformed data is additionally smoothed with a small Gaussian window. The two maps have the same size and number of pixels ($55\times55\,nm^2$, 288×288 pixels), and are acquired on two different field of views about 100 nm apart from each other. They have different setup conditions (V_b, I_t) and energy ranges: (50 meV, 500 pA) and [−50 meV; 50 meV] for Fig. 6.7a-b versus (−50 meV, 500 pA) and [−15 meV; 15 meV] for Fig. 6.7c-d[4].

The main features in the cuts can be recognized as the dispersing scattering vectors that we identified in Sec. 6.4. In order to extract quantitative information, we individually plot every dispersion as intensity vs. momentum curves for all energies, as shown in Fig. 6.7f for the β_X scattering from Fig. 6.7c. This leads to the STM analogous of ARPES momentum distribution curves (MDCs). We can then fit the data with a gaussian curve summed with a linear background, to extract the peak position. The dispersion of all the scattering vectors extracted by fitting the peak positions are plotted in Fig. 6.7g-h for both the datasets in the two different directions. Sometimes the signal is not very clear, causing a considerable uncertainty in the determination of the peak position. This mostly happens when two dispersions cross each other or when they flatten out.

By fitting the dispersions with a linear curve (or with a parabolic curve for the α and β_X hole pockets), we can extract the magnitude q_F of all the q-vectors at the Fermi level. Moreover, for scattering within one single band, the Fermi velocity can be obtained from the slope of the fit. In the next section, we will compare both quantities with photoemission data.

[4] The cuts in Fig. 6.7c-d are extracted from the same measurement of which we showed conductance layers and Fourier transforms in Fig. 6.4 and Fig. 6.6.

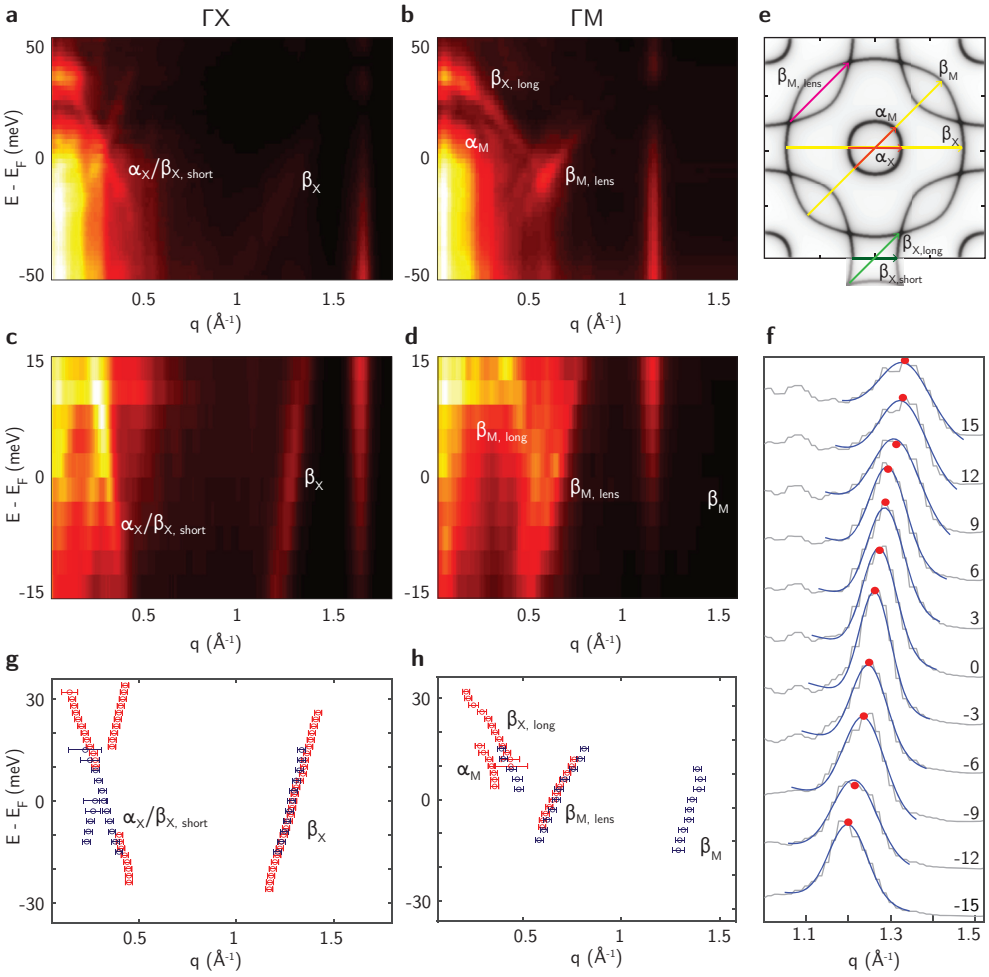

Figure 6.7: **a-b**, Cuts of a spectroscopic map with (V_b, I_t) = (50 meV, 500 pA) and energy range [-50 meV, 50 meV], along ΓX and ΓM directions. **c-d**, Cuts of a spectroscopic map with (V_b, I_t) = (-50 meV, 500 pA) and energy range [-15 meV, 15 meV], along ΓX and ΓM directions. **e**, Fermi surface from tight-binding model with identification of the main scattering vectors. **f**, Example of a gaussian fit to the QPI MDCs for the β_X scattering from panel **c**. The energies are indicated in meV units. **g-h**, Dispersions extracted from panels **a-b** (in red) and **c-d** (in blue) through fits analogous to the one shown in panel **f**. The error bars are the quadratic sum of the standard deviations extracted from the fit and the size of the smoothing window.

6.6 Comparison with ARPES

In Table 6.1, we compare the values obtained from STM data for q_F and v_F with the corresponding values obtained with ARPES in Ref. [69]. In general, we find very good agreement for what concerns the magnitude of the scattering vectors at the Fermi level, while the Fermi velocities agree less well. The values for the Fermi velocities obtained in the ΓM direction are not very reliable, due to poor S/N. However, also in the ΓX direction, where the STM signal is clear, the ARPES-derived value is about 10% larger.

In Fig. 6.8, we plot the superposition of our STM results with ARPES results from Ref. [68, 69], in order to have a further visual comparison. The STM q-axis are rescaled by a factor two, to coincide with the ARPES data.

In Fig. 6.8a, we compare the Fermi surfaces derived from ARPES and STM. We can obtain the Fermi surface for the β band from the STM data shown in Fig. 6.6e by fitting intensity profiles radially for several angles between ΓX and ΓM. We plot the values of k_F extracted in this way as datapoints above the measured ARPES Fermi surface. The two colors correspond to the two different measurements, with the respective standard deviations. The agreement is good in all directions.

		STM	ARPES
q_F (Å^{-1})	α_X	0.32*	0.32
	α_M	0.38	0.35
	β_X large	1.29	1.28
	β_M large	1.37	1.36
	β_X short	0.32*	0.34
	β_X long	0.53	0.52
	β_M lens	0.66	0.63
	$\alpha - \beta$	0.56	0.52
v_F (eV Å)	α_X	0.39*	0.41
	α_M	0.35**	0.41
	β_X short	0.39*	0.55
	β_X - large	0.46	0.55
	β_M - large	0.50**	0.61

Table 6.1: Comparison of scattering vectors q_F and velocities v_F at the Fermi level as obtained from STM (this study) and ARPES (Ref. [69]). The STM values, when possible, are averaged between the two datasets. The single asterisk indicates that the identification of the STM feature is uncertain, and could belong to both the α_X pocket and the β_X square pocket. The double asterisk indicates that the STM data is not fully reliable due to poor data quality.

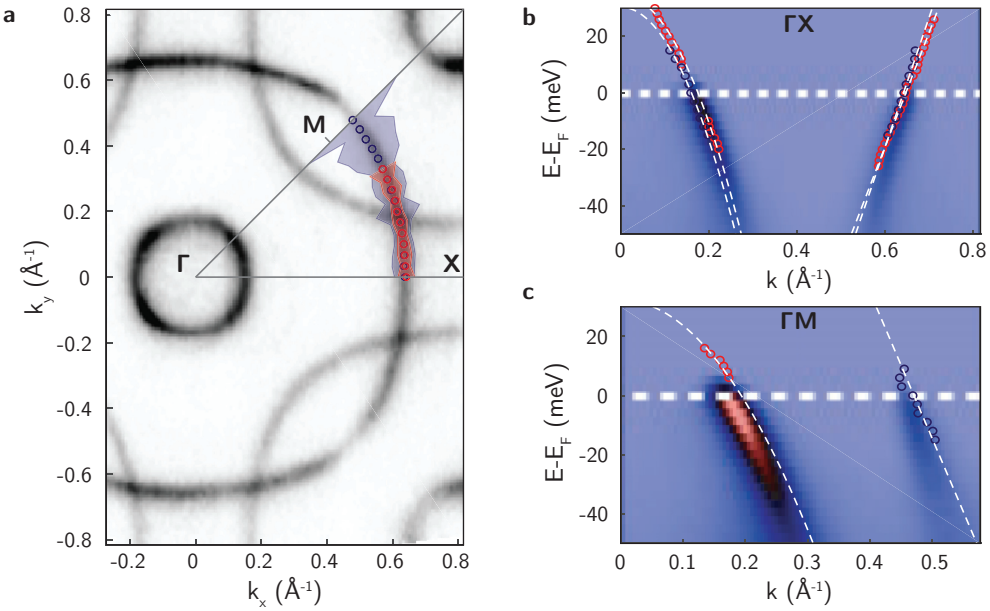

Figure 6.8: Comparison of STM and ARPES results. **a**, STM-derived Fermi surface (in circles) plotted over the ARPES Fermi surface (Ref. [69]). The STM points are obtained from radial cuts of the Fourier-transformed QPI signal between the ΓX and ΓM directions. The two STM datasets are given with different colors, and the shaded areas indicate the standard deviations. **b-c**, Superposition of the ARPES dispersions (adapted from Ref. [68]) and the STM dispersions in the ΓX and ΓM directions, respectively. The data points are indicated by circles with different colors for the two datasets, and the white dash lines are fits to the STM data. The STM dispersions are renormalized by dividing the k-axis by a factor two.

In Fig. 6.8b-c, we plot the comparison of the dispersions. For the STM data, we plot both the peak positions as in Fig. 6.7g-h and the linear or parabolic fits (white dashed lines) from which we extract the Fermi velocities. As already anticipated by the values in Table 6.1, the STM-derived dispersions are generally flatter than the ones obtained with ARPES. For what concerns the α band, the dispersions agree better, however, mostly in the ΓM direction, the STM dispersion is a bit displaced with respect to the ARPES data. For the β band, the dispersions clearly deviate from each other, with most differences visible along ΓM. As we already indicated before, along this direction the STM signal is suppressed, resulting in worse data quality.

A good agreement of the Fermi surface, but flatter STM dispersions with respect to the ARPES ones, have been encountered before, for instance on Sr_2RuO_4 [43] (which is a very similar system to Sr_2RhO_4) and on cuprates [18, 47]. For cuprates, some efforts have been made to understand the discrepancies [47]. It has been suggested that both tunneling and photoemission matrix elements could play a role. Indeed,

the dispersions agree better when ARPES experiments are performed with a photon polarization that suppresses states in the same direction as they are suppressed in STM [47].

To bring the comparison with ARPES further, one could try to extract the self energy from QPI data, as it is proposed in Ref. [149]. To do so, one needs to fit the STM MDCs with Lorentzian curves, and extract the position of the peaks and their width. However, data of outstanding quality is necessary for this type of analysis. We preliminary extracted the self energy for the β band, leading to results that are in rough agreement with ARPES. However, a more detailed analysis on better quality datasets is needed in order to draw firm conclusions.

6.7 Conclusions

We are certain that it is important to be able to compare STM with ARPES results. Both techniques have their own strengths, and combining their complementary results can lead to crucial insights into the understanding of quantum materials. However, we think that this combination is reliable only if the techniques deliver similar results when they measure the same quantities on simple materials, or if we understand well where possible discrepancies come from.

In this chapter, we show QPI measurements on the correlated metal Sr_2RhO_4, which seems like a good candidate to test the comparison between STM and ARPES. While the data quality and statistics is not yet good enough to come to sound conclusions, we obtain some promising, preliminary results.

We are able to identify all the features observed with STM as scattering between different areas of the Fermi surface, and we obtain very good agreement for the magnitude of the scattering vectors at the Fermi level. The values obtained for the Fermi velocities are instead agreeing less well with ARPES results. Interestingly, a comparable disagreement for the Fermi velocity is reported for Sr_2RuO_4 [43], which in many ways is a very similar system to Sr_2RhO_4. This might indicate a deeper origin for the disagreement, and further investigations on both systems could, for instance, indicate if they are due to the nature of the scatterers or to the measurement technique.

The quality of the Sr_2RhO_4 data presented here is possibly still affected by some measurement artifacts, and hence, we cannot yet infer the origin of this disagreement. We are planning further measurements that should lead to better results, in addition to more statistics. This will be achieved, for instance, by setting up the measurements at negative biases to avoid artifacts (following the suggestions of Ref. [150]), by reducing the energy resolution to 1.5 meV (best resolution achievable at 4.3 K), and eventually

by exploring a bigger negative energy range. Moreover, a better tip quality should help to get clearer data.